The Astrophysical Journal, 770:139 (10pp), 2013 June 20 doi:10.1088/0004-637X/770/2/139

COMPOSITION OF LOW-REDSHIFT HALO GAS

Renyue Cen
Department of Astrophysical Sciences, Princeton University, Peyton Hall, Ivy Lane, Princeton, NJ 08544, USA; cen@astro.princeton.edu
Received 2012 December 6; accepted 2013 April 11; published 2013 June 5

ABSTRACT

Halo gas in low-z ($z < 0.5$) $\geqslant 0.1\,L_*$ galaxies in high-resolution, large-scale cosmological hydrodynamic simulations is examined with respect to three components: cold, warm, and hot with temperatures of $<10^5$, 10^{5-6}, and $>10^6$ K, respectively. Utilizing O VI $\lambda\lambda$1032, 1038 absorption lines, the warm component is compared to observations, and agreement is found with respect to the galaxy–O VI line correlation, the ratio of the O VI line incidence rate in blue to red galaxies, and the amount of O VI mass in star-forming galaxies. A detailed account of the sources of warm halo gas (stellar feedback heating, gravitational shock heating, and accretion from the intergalactic medium), inflowing and outflowing warm halo gas metallicity disparities, and their dependencies on galaxy types and environment is also presented. With the warm component securely anchored, our simulations make the following additional predictions. First, cold gas is the primary component in inner regions with its mass comprising 50% of all gas within galactocentric radius $r = (30, 150)$ kpc in (red, blue) galaxies. Second, at $r > (30, 200)$ kpc in (red, blue) galaxies the hot component becomes the majority. Third, the warm component is a perpetual minority, with its contribution peaking at ∼30% at $r = 100$–300 kpc in blue galaxies and never exceeding 5% in red galaxies. The significant amount of cold gas in low-z early-type galaxies, which was found in simulations and in agreement with recent observations (Thom et al.), is intriguing, as is the dominance of hot gas at large radii in blue galaxies.

Key words: cosmology: theory – galaxies: halos – hydrodynamics – intergalactic medium – supernovae: general

Online-only material: color figures

1. INTRODUCTION

Galaxy formation and evolution is the central astrophysical problem in cosmology. The basic parameters of the cosmological framework—the standard cosmological constant-dominated cold dark matter (DM) model (LCDM; e.g., Krauss & Turner 1995; Bahcall et al. 1999)—are largely fixed to an accuracy of ∼10% or better. The LCDM model is able to explain a variety of observations on scales greater than ∼1 Mpc, including high-redshift supernovae (e.g., Perlmutter et al. 1998; Riess et al. 1998; Astier et al. 2006), the cosmic microwave background (e.g., Komatsu et al. 2011; Planck Collaboration et al. 2013), the large-scale distribution of galaxies (e.g., Tegmark et al. 2004; Percival et al. 2007), X-ray cluster abundance (e.g., Allen et al. 2008), and the Lyα forest (e.g., Croft et al. 2002; Seljak et al. 2005).

An important component of the astrophysical problem—the gravitational formation and evolution of halos that host galaxies—is well understood through N-body simulations (e.g., Jenkins et al. 2001; Bullock et al. 2001; Wechsler et al. 2002; Diemand et al. 2007) and analytic models (e.g., Bond et al. 1991; Lacey & Cole 1993; Sheth & Tormen 1999; Mo & White 2002; Cooray & Sheth 2002). The gastrophysics of galaxy formation and feedback, on the other hand, is far from being adequately understood. Alternative approaches that parameterize and then infer physical processes based on finding the best matches to observations, such as semi-analytic methods (e.g., Somerville & Primack 1999; Benson et al. 2003) and the halo-occupation distribution method (e.g., Berlind & Weinberg 2002; Zheng et al. 2007), have been successful but have limited predictive power. More importantly, in semi-analytic methods the treatment of galaxy formation is halo based and largely decoupled from that of the intergalactic medium (IGM), which in fact has dramatically evolved with time. At $z = 2$–6 most of the baryons are found to be in the Lyα forest, a relatively cold temperature phase at $\sim 10^4$ K, as indicated by both observations (e.g., Rauch et al. 1997) and simulations (e.g., Cen et al. 1994). By $z = 0$ most of the baryons in the IGM have been heated up, primarily by gravitational shocks, to temperatures that broadly peak at about 10^6 K, the so-called warm-hot intergalactic medium (WHIM; e.g., Cen & Ostriker 1999). The "ab initio," more predictive approach of direct cosmological hydrodynamic simulations, after having made steady progress (e.g., Evrard et al. 1994; Katz et al. 1996; Teyssier 2002; Kereš et al. 2005; Hopkins et al. 2006; Oppenheimer & Davé 2006; Governato et al. 2007; Naab et al. 2007; Gnedin et al. 2009; Joung et al. 2009; Cen 2011), begin to be able to make statistically significant and physically realistic characterizations of the simultaneous evolution of galaxies and the IGM.

The aim of this paper is to quantify the composition of halo gas in low-redshift galaxies, using state-of-the-art high-resolution ($460\,h^{-1}$ pc), large-scale (thousands of galaxies) cosmological hydrodynamic simulations with advanced treatments of star formation, feedback, and microphysics. Here our focus is on gas that is in the immediate vicinities of galaxies, within galactocentric distances of 10–500 kpc, where the exchanges of gas, metals, energy, and momentum between galaxies and the IGM primarily take place. We shall broadly term it "circumgalactic medium (CGM)" or "halo gas." Understanding halo gas is necessary before a satisfactory theory of galaxy formation and evolution may be constructed. The present theoretical study is also strongly motivated observationally in light of the recent rapid accumulation of data by *Hubble Space Telescope* (*HST*) observations, which enable detailed comparisons between galaxies and the warm component ($T \sim 10^5$–10^6 K) of their CGM at low redshift (e.g., Chen & Mulchaey 2009; Prochaska et al. 2011b; Tumlinson et al. 2011a; Tripp et al. 2011).

We shall dissect halo gas at low redshift ($z < 0.5$) into three components: cold, warm, and hot gas with temperatures of $<10^5$, 10^5–10^6, and $>10^6$ K, respectively. A large portion of our presentation is spent on quantifying O VI $\lambda\lambda$1032, 1038 absorption lines and the overall properties of warm halo gas and comparing them to observations in as much detail as possible. Feedback processes, while being treated with increased physical sophistication, are still not based on first principles due primarily to resolution limitations in large-scale cosmological simulations. Thus, it is imperative that our simulations are well validated and anchored by requiring that some key and pertinent aspects of our simulations match relevant observations. The O VI line, when collisionally ionized, has its abundance peaked at a temperature of $T = 10^{5.3-5.7}$ K and thus is an excellent proxy for the warm gas. After validating our simulations with respect to the observed properties of O VI absorption lines, we present the overall composition of low-redshift halo gas. We find that, for (red, blue) galaxies more luminous than 0.1 L_*, the cold gas of $T < 10^5$ K, on average, dominates the halo gas budget within a radius of (30, 150) kpc. Beyond a radius of (30, 200) kpc for (red, blue) galaxies, the hot gas of $T > 10^6$ K dominates. The warm component remains the smallest minority at all radii, peaking at $\sim$30% at $\sim$100–300 kpc for blue galaxies but never exceeding 5% for red galaxies.

The following physical picture emerges for the physical nature of the warm gas component. The warm halo gas has a cooling time much shorter than the Hubble time and hence is "transient," with their presence requiring sources. To within a factor of two we find that for low-z $\geqslant 0.1$ L_* red galaxies, contributions to warm halo gas from star formation feedback (F_r), accretion of intergalactic medium (A_r), and gravitational shock heating (G_r) are $(F_r, A_r, G_r) = (30\%, 30\%, 40\%)$. For blue $\geqslant 0.1$ L_* galaxies, contributions to warm halo gas from the three sources are $(F_b, A_b, G_b) = (48\%, 48\%, 4\%)$. The mean metallicity of warm halo gas in (red, blue) galaxies is ($\sim 0.25\ Z_\odot$, $\sim 0.11\ Z_\odot$). The environmental dependence of O VI-bearing halo gas is as follows. In low-density environments, the metallicity of inflowing warm gas is substantially lower than that of outflowing warm gas; the opposite is true in high-density environments.

The outline of this paper is as follows. In Section 2.1 we detail the simulation parameters and hydrodynamic code, followed by a description of our method of making synthetic O VI spectra in Section 2.2. This is followed by a description of how we average the two separate simulations, C (cluster) and V (void), run in Section 2.3. The results are presented in Section 3. A detailed comparison of the galaxy–O VI absorber correlation is computed and shown to match observations in Section 3.1, followed in Section 3.2 by an analysis of the ratio of O VI absorber incidence rates around blue and red galaxies that is found to be consistent with observations. A detailed examination of the physical origin and properties of the warm gas in a low-z halo is given in Section 3.3. The overall composition of low-z halo gas is given in Section 3.4 and conclusions are summarized in Section 4.

2. SIMULATIONS

2.1. Hydrocode and Simulation Parameters

We perform cosmological simulations with the adaptive mesh refinement Eulerian hydrocode, Enzo (Bryan 1999; Bryan & Norman 1999; O'Shea et al. 2005). The version we use is a "branch" version (Joung et al. 2009), which includes a multi-tiered refinement method that allows for spatially varying maximum refinement levels, when desired. This Enzo version also includes metallicity-dependent radiative cooling extended down to 10 K, molecular formation on dust grains, photoelectric heating, and other features that are different from or not in the public version of the Enzo code. We use the following cosmological parameters that are consistent with the *WMAP*7-normalized (Komatsu et al. 2011) LCDM model: $\Omega_M = 0.28$, $\Omega_b = 0.046$, $\Omega_\Lambda = 0.72$, $\sigma_8 = 0.82$, $H_0 = 100\,h\,\mathrm{km\,s^{-1}\,Mpc^{-1}} = 70\,\mathrm{km\,s^{-1}\,Mpc^{-1}}$, and $n = 0.96$. These parameters are also consistent with the latest *Planck* results (Planck Collaboration et al. 2013) if one adopts the Hubble constant, which is the average of the *Planck* value and the values derived from the Type Ia supernovae and *HST* key program (Riess et al. 2011; Freedman et al. 2012). We use the power spectrum transfer functions for cold DM particles and baryons using fitting formulae from Eisenstein & Hut (1998). We use the Enzo inits program to generate the initial conditions.

First, we ran a low-resolution simulation with a periodic box of $120\,h^{-1}$ Mpc on the side. We identified two regions separately, one centered on a cluster of mass the size of $\sim 2 \times 10^{14}\ M_\odot$ and the other centered on a void region at $z = 0$. We then resimulate each of the two regions separately with a high resolution, but embedded in the outer $120\,h^{-1}$ Mpc box to properly take into account the large-scale tidal field and appropriate boundary conditions at the surface of the refined region. We name the simulation centered on the cluster the "C" run and that centered on the void the "V" run. The refined region for the "C" run has a size of $21 \times 24 \times 20\,h^{-3}$ Mpc^3 and the size of the "V" run is $31 \times 31 \times 35\,h^{-3}$ Mpc^3. At their respective volumes, they represent 1.8σ and -1.0σ fluctuations. The root grid has a size of 128^3 with 128^3 DM particles. The initial static grids in the two refined boxes correspond to a 1024^3 grid on the outer box. The initial number of DM particles in the two refined boxes corresponds to 1024^3 particles on the outer box. This translates into an initial condition in the refined region with a mean interparticle separation of $117\,h^{-1}$ kpc comoving and a DM particle mass of $1.07 \times 10^8\,h^{-1}\,M_\odot$. The refined region is surrounded by two layers (each of $\sim 1\,h^{-1}$ Mpc) of buffer zones with particle masses successively larger by a factor of eight for each layer, which then connects with the outer root grid that has a DM particle mass 8^3 times that of the refined region. The initial density fluctuations are included up to the Nyquist frequency in the refined region. The surrounding volume outside the refined region is also followed hydrodynamically, which is important in order to properly capture matter and energy exchanges at the boundaries of the refined region. Because we still cannot run a very large volume simulation with adequate resolution and physics, we choose these two runs of moderate volumes to represent two opposite environments that possibly bracket the universal average.

We choose a varying mesh refinement criterion scheme where the resolution is always better than 460 h^{-1} proper parsecs within the refined region and corresponds to a maximum mesh refinement level of 9 above $z = 3$, of 10 at $z = 1$–3, and 11 at $z = 0$–1. The simulations include a metagalactic UV background (Haardt & Madau 2012) and a model for shielding UV radiation with atoms (Cen et al. 2005). The simulations also include metallicity-dependent radiative cooling and heating (Cen et al. 1995). We clarify that our group has included metal cooling and metal heating (due to photoionization of metals) in all our studies since Cen et al. (1995) to avoid all doubt (e.g., Wiersma et al. 2009; Tepper-García et al. 2011). Star particles are created in cells that satisfy a set of criteria for star formation proposed by Cen & Ostriker

(1992). Each star particle is tagged with its initial mass, creation time, and metallicity; star particles typically have masses of $\sim 10^{5-6}\,M_{\odot}$.

Supernova feedback from star formation is modeled following Cen et al. (2005). Feedback energy and ejected metal-enriched mass are distributed into 27 local gas cells centered at the star particle in question, weighted by the specific volume of each cell (i.e., weighting is equal to the inverse of density), which is to mimic the physical process of supernova blast wave propagation, which tends to channel energy, momentum, and mass into the least dense regions (with the least resistance and cooling). We allow the whole feedback processes to be hydrodynamically coupled to surroundings and subject to relevant physical processes, such as cooling and heating, as in nature. The extremely inhomogeneous metal enrichment process demands that both metals and energy (and momentum) are correctly modeled so that they are transported in the right direction in a physically sound (albeit still approximate at the current resolution) way, at least in a statistical sense. In our simulations, metals are followed hydrodynamically by solving the metal density continuity equation with sources (from star formation feedback) and sinks (due to subsequent star formation). Thus, metal mixing and diffusion through advection, turbulence, and other hydrodynamic processes are properly treated in our simulations.

The primary advantages of this supernova energy-based feedback mechanism are three-fold. First, nature does drive winds in this way and the energy input is realistic. Second, it has only one free parameter, $e_{\rm SN}$, namely, the fraction of the rest mass energy of stars formed that is deposited as thermal energy on the cell scale at the location of supernovae. Third, the processes are treated physically, obeying their respective conservation laws (where they apply), allowing the transport of metals, mass, energy, and momentum to be treated self-consistently, and taking into account relevant heating/cooling processes at all times. We use $e_{\rm SN} = 1 \times 10^{-5}$ in these simulations. The total amount of explosion kinetic energy from Type II supernovae with a Chabrier initial mass function (IMF) translates into $e_{\rm SN} = 6.6 \times 10^{-6}$. Observations of local starburst galaxies indicate that nearly all of the star formation-produced kinetic energy (due to Type II supernovae) is used to power galactic superwinds (e.g., Heckman 2001). Given the uncertainties on the evolution of IMF with redshift (i.e., possibly more top heavy at higher redshift) and the fact that newly discovered prompt Type I supernovae contribute a comparable amount of energy compared to Type II supernovae, it seems that our adopted value for $e_{\rm SN}$ is consistent with observations and physically realistic. The validity of this thermal energy-based feedback approach comes empirically. In Cen (2012b), the metal distribution in and around galaxies over a wide range of redshift ($z = 0$–5) is shown to be in excellent agreement with respect to the properties of observed damped Lyα systems (Rafelski et al. 2012), whereas in Cen (2012a) we further show that the properties of O VI absorption lines at low redshift, including their abundance, Doppler-column density distribution, temperature range, metallicity, and coincidence between O VII and O VI lines, are all in good agreement with observations (Danforth & Shull 2008; Tripp et al. 2008; Yao et al. 2009). This is not trivial by any means because they require that the transport of metals and energy from galaxy star formation sites to megaparsec scale be correctly modeled as a function of distance over the entire cosmic timeline, at least in a statistical sense.

2.2. Simulated Galaxy Catalogs

We identify galaxies in our high-resolution simulations using the HOP algorithm (Eisenstein & Hu 1999) operated on stellar particles, which was tested and found to be robust and insensitive to specific choices of concerned parameters within reasonable ranges. Satellites within a galaxy are clearly identified separately. The luminosity of each stellar particle at each of the five Sloan Digital Sky Survey (SDSS) bands is computed using the GISSEL (Galaxy Isochrone Synthesis Spectral Evolution Library) stellar synthesis code (Bruzual & Charlot 2003) by supplying the formation time, metallicity, and stellar mass. Collecting luminosity and other quantities of member stellar particles, gas cells, and DM particles yields the following physical parameters for each galaxy: position, velocity, total mass, stellar mass, gas mass, mean formation time, mean stellar metallicity, mean gas metallicity, star formation rate (SFR), luminosities in five SDSS bands (ugriz), and others. At a spatial resolution of proper 460 pc h^{-1} with more than 2000 well-resolved galaxies at $z = 0$, this simulated galaxy catalog presents an excellent (by far the best available) tool to study CGM around galaxies at low redshift.

In some of the analysis we perform here, we divide our simulated galaxy sample into two sets according to the galaxy color. We shall call galaxies with $g - r < 0.6$ blue and those with $g - r > 0.6$ red. We found that $g - r = 0.6$ is at the trough of the galaxy bimodal color distribution of our simulated galaxies (Cen 2011; Tonnesen & Cen 2012), which agrees well with that of observed low-z galaxies (e.g., Blanton et al. 2003).

2.3. Generation of Synthetic O VI Absorbers

The photoionization code CLOUDY (Ferland et al. 1998) is used post-simulation to compute the abundance of O VI. We adopt the shape of the UV background calculated by Haardt & Madau (2012) normalized by the intensity at 1 Ryd determined by Shull et al. (1999) and assume ionization equilibrium. We generate synthetic absorption spectra given the density, temperature, metallicity, and velocity fields in simulations. Each absorption line is identified by the velocity (or wavelength) interval between one downward-crossing and the next upward-crossing points at a flux equal to 0.99 (a flux equal to unity corresponds to an unabsorbed continuum flux) in the spectra. We do not add instrumental and other noises to the synthetic spectra. Since the absorption lines in question are sparsely distributed in the velocity space, their identifications have no significant ambiguity. Column density, equivalent width, Doppler width, mean column density-weighted velocity and physical space locations, mean column density-weighted temperature, density, and metallicity are computed for each line. We sample the C and V runs, respectively, with 72,000 and 168,000 random lines of sight at $z = 0$, with a total path length of $\Delta z \sim 2000$. A total of $\sim$30,000 $\geqslant$ 50 mA O VI absorbers are identified in the two volumes. While a detailed Voigt profile fitting of the flux spectrum would have enabled a closer comparison with observations, simulations suggest that such an exercise does not necessarily provide a better physical understanding of the absorber properties, because bulk velocities are very important and velocity substructures within an absorber do not necessarily correspond to separate physical entities (Cen 2012a).

2.4. Averaging C and V Runs

The C and V runs at $z = 0$ are used to obtain an "average" of the universe. This cannot be done precisely without much

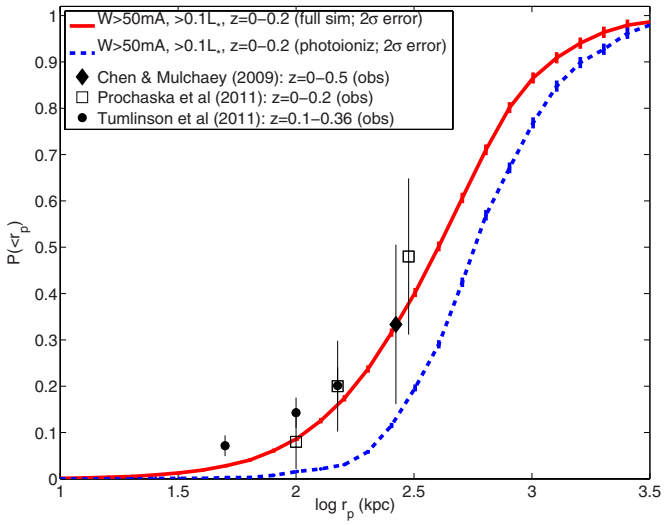

Figure 1. Cumulative probability distribution functions of $\geqslant$50 mA O VI absorbers of finding $\geqslant$0.1 L_* galaxies at $z = 0$–0.2 from simulations with 2σ error bars (red solid curves). The distribution functions at $z = 0$–0.2 are obtained by averaging $z = 0$ and $z = 0.2$ results with equal weighting. Also shown as symbols are observations from Chen & Mulchaey (2009; solid diamonds), Prochaska et al. (2011a; open squares), and Tumlinson et al. (2011b; solid dots). Because the impact parameter of samples from Tumlinson et al. (2011b) reaches only 150 kpc, we have normalized their data points by matching their $r_p = 150$ kpc point to the $r_p = 150$ kpc point of Prochaska et al. (2011a). The blue dashed line is produced only when photoionized O VI lines with temperature $T \leqslant 3 \times 10^4$ K in our simulations are used. The χ square per degree of freedom for the red solid line using all observed data points is 1.2 whereas it is 7.6 for the blue dashed line.

(A color version of this figure is available in the online journal.)

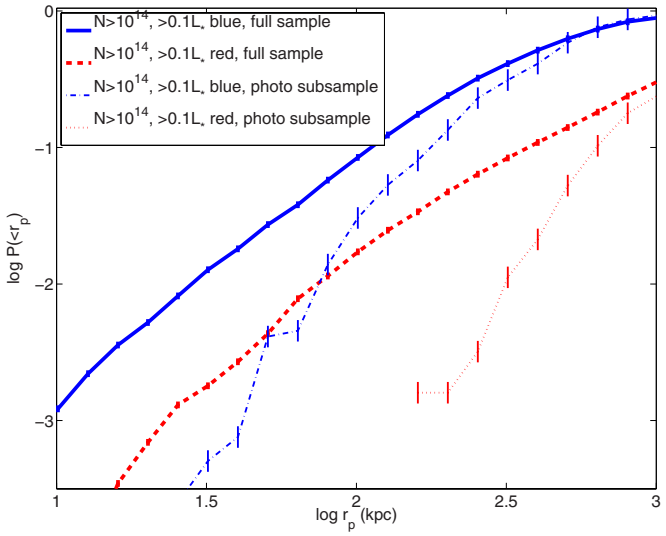

Figure 2. Cumulative probability distribution functions of O VI absorbers with a column density greater than 10^{14} cm^{-2} of finding a (red, blue) galaxy of luminosity of $\geqslant$0.1 L_* (in the SDSS r band) at $z = 0.2$ with (red dashed, blue solid) lines from simulations with 10σ error bars. The red dotted line and blue dot-dashed line are the corresponding functions for the subset of O VI absorbers that have temperature $T \leqslant 3 \times 10^4$ K in our simulations.

(A color version of this figure is available in the online journal.)

larger simulation volumes, which is presently not feasible. Nevertheless, we make the following attempt to obtain an approximate average. The number density of galaxies with luminosity greater than 0.1 L_* in the SDSS r band in the two runs is found to be $3.95 \times 10^{-2}\ h^3$ Mpc^{-3} and $1.52 \times 10^{-2}\ h^3$ Mpc^{-3}, respectively, in the C and V boxes. We fix the weighting for the C and V runs in order to average the statistics of the C and V runs by requiring that the average density of galaxies with luminosity greater than 0.1 L_* in the SDSS r band in the simulations are equal to the observed global value of $2.87 \times 10^{-2}\ h^3$ Mpc^{-3} by SDSS (Blanton et al. 2003). In the results shown below, we use this method to obtain averages of the statistics, where doing so allows for some more quantitative comparisons with observed data.

3. RESULTS

3.1. Galaxy–O VI Absorber Correlation at $z = 0$–0.5

Figure 1 shows the cumulative probability distribution functions of $\geqslant$50 mA O VI absorbers for finding $\geqslant$0.1 L_* galaxies at $z = 0$–0.2 from simulations as well as observations. We find good agreement between simulations and observations, quantified by the χ square per degree of freedom of 1.2. In comparison, if we use only the low-temperature ($T < 3 \times 10^4$ K) O VI absorbers in the simulations, the cumulative probability is no longer in reasonable agreement with observations, with the χ square per degree of freedom being equal to 7.6; this exercise, however, only serves as an illustration of what a photoionization-dominated model may produce. It will be very interesting to make a similar calculation directly using smoothed particle hydrodynamic (SPH) simulations that have predicted the dominance of photoionized O VI absorbers even for strong O VI absorbers as shown here (e.g., Oppenheimer et al. 2012).

The significant difference found with respect to the strong O VI absorber–galaxy cross-correlations between the photoionization and collisional ionization-dominated models stems from the relative difference in the locations of strong O VI absorbers in the two models. In the collisional ionization-dominated model (Cen 2012a; Shull et al. 2012), the strong O VI absorbers are spatially closer to galaxies in order to have a high enough temperature (hence high O VI abundance) and a high enough density to make strong O VI absorbers, whereas in the photoionization-dominated model (Oppenheimer et al. 2012), they have to be sufficiently far from galaxies to have low enough densities to be photoionized to O VI. An additional requirement in the latter for the production of strong O VI absorbers is high metallicity ($\geqslant$0.1 $Z_\odot$) to yield high enough O VI columns, as found in SPH simulations (Oppenheimer et al. 2012).

3.2. O VI Absorbers Around Blue and Red Galaxies

Observations have shown an interesting dichotomy between the O VI incidence rates of blue and red galaxies. Figure 2 shows the cumulative probability distribution functions of $N_{\rm O\,VI} > 10^{14}$ cm^{-2} O VI absorbers for finding a (red, blue) galaxy of luminosity of $\geqslant$0.1 L_* at $z = 0.2$ from simulations. In Figure 3, we show the ratio of the cumulative radial distribution per red galaxy to that per blue galaxy of $\geqslant$0.1 L_* at $z = 0.2$, compared to observations. Figure 3 shows that in the $r = 50$–300 kpc range, the ratio of the incidence rate of strong O VI absorbers around red galaxies to that around blue galaxies is about 1:5, which is in quantitative agreement with observations. In the case with photoionized O VI absorbers only, the fraction of O VI absorbers around red galaxies is much lower and lies significantly below the observational estimates, although the current small observational sample prevents us from reaching strong statistical conclusions based on this ratio alone.

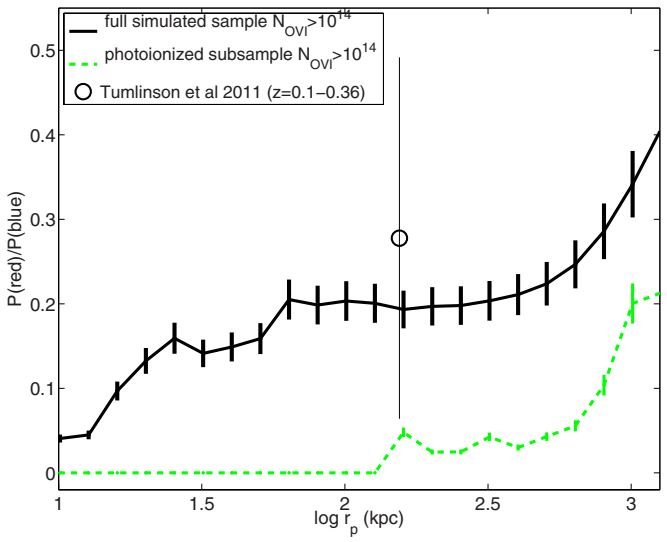

Figure 3. Ratio of the cumulative radial probability distribution function of O VI absorbers with an equivalent width (W) greater than 50 mA per red galaxy to that per blue galaxy of $\geqslant 0.1\ L_*$ (in the SDSS r band) at redshift $z = 0.2$ from simulations (the black solid curve, 2σ error bars). The same ratio for photoionized O VI absorbers ($T \leqslant 3 \times 10^4$ K) only is shown as the green dashed curve. Also shown as an open circle is the observation by Tumlinson et al. (2011b).

(A color version of this figure is available in the online journal.)

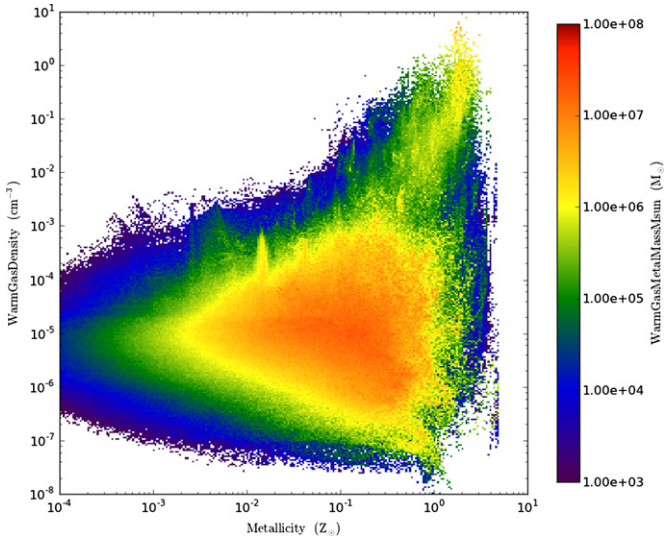

Figure 4. Metal mass in the warm gas ($T = 10^5$–10^6 K) distributed in the density–metallicity phase space. This is a good proxy for O VI-bearing gas. The amount of gas mass in the WHIM is 40% of the total gas in the simulation volume.

(A color version of this figure is available in the online journal.)

We see in Figure 2 that statistical uncertainties for the radial probability distribution of simulated O VI absorbers are already very small due to a significant number of simulated galaxies and a still larger number of simulated absorbers used. What limits us from making firm statistical statements is the sample size of observational data. Hypothetically, if the mean remains the same, a factor of two smaller error bars would render the photoionization-dominated model inconsistent with observations at $\geqslant 2\sigma$ confidence level, whereas our collisionally dominated model would be consistent with observations within 1σ.

3.3. Physical Origin of O VI Absorbers

We now turn to analysis to give a physical description for the origin of O VI absorbers in the CGM in the context of the cold dark matter model. While this section is interesting on its own for physically understanding halo gas, the next section on halo gas mass decomposition is not predicated on it.

First, we ask whether the warm gas traced by O VI absorbers requires significant energy input to be sustained over the Hubble time. Figure 4 shows the metal mass in the warm gas ($T = 10^5$–10^6 K) distributed in the density–metallicity phase space. We see that most of the warm metals are concentrated in a small phase space region centered at $(n, Z) = (10^{-5}\ \mathrm{cm}^{-3}, 0.15\ Z_\odot)$. We note that the amount of gas mass in the WHIM is 40% of the total gas averaged over the simulation, which is in agreement with previous simulations (e.g., Cen & Ostriker 1999, 2006; Davé et al. 2001) and other recent simulations (Smith et al. 2011; Davé et al. 2010; Shen & Kelly 2010; Tornatore et al. 2010). For this gas we find that the cooling time is $t_{\rm cool} = 6 \times 10^8$ yr (assuming a temperature of $10^{5.5}$ K), shorter than the Hubble time by a factor of $\geqslant 20$. For the strong O VI absorbers considered here, the cooling time is still shorter. In other words, either (1) energy is supplied to sustain existing O VI gas, (2) new warm gas is accreted, or (3) some hotter gas needs to continuously cool through the warm phase. Since O VI gas by itself does not define a set of stable systems and is spatially well mixed or in close proximity to other phases of gas, this suggests that the O VI gas in halos is *"transient"* in nature.

We consider three sources of warm halo gas: mechanical feedback energy from stellar evolution, gravitational binding energy released from halo formation and interactions, and direct accretion from the IGM. This simplification sets a framework to make a quantitative assessment of these three sources for warm gas that we now describe. We denote by F_b and F_r the O VI incident rate (in some convenient units) per blue and red $\geqslant 0.1\ L_*$ galaxy due to star formation feedback energy heating, by G_b and G_r those due to gravitational heating, and by A_b and A_r those due to accreted gas from the IGM. It is useful to stress the distinction between G and A. A is gas directly accreted from IGM that is either already warm or heated up to be warm by compression upon accretion onto the halo. On the other hand, G is gas that is shock heated to the warm phase or to a hotter phase that cools back down to become warm. Restricting our analysis to within a galactocentric radius of 150 kpc and reading off numbers from the red curve in Figure 3, we obtain two relations:

$$F_b + G_b + A_b = 5,$$
$$F_r + G_r + A_r = 1. \quad (1)$$

An additional reasonable assumption is now made: feedback heating rate S_r (S_b) is proportional to the average $\mathrm{SFR_r}$ ($\mathrm{SFR_b}$), which in turn is proportional to their respective gas accretion rate A_r (A_b). This assumption allows us to lump F_r and A_r (F_b and A_b):

$$S_b = F_b + A_b = C \times \mathrm{SFR_b}$$
$$S_r = F_r + A_r = C \times \mathrm{SFR_r}, \quad (2)$$

where C is a constant. We will return to determine F_r and A_r (F_b and A_b) separately later. Equation (1) is now simplified to

$$S_b + G_b = 5,$$
$$S_r + G_r = 1. \quad (3)$$

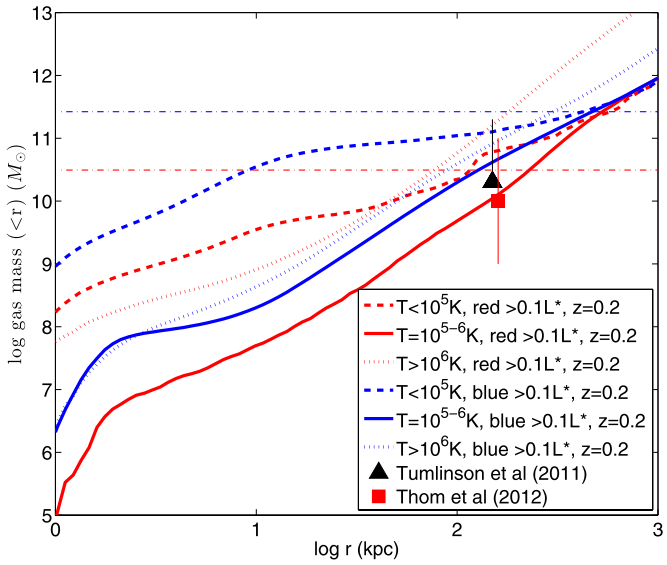

Figure 5. Cumulative gas mass as a function of radius for cold (dashed curves), warm-hot (solid curves), and hot gas (dotted curves) around blue (blue curves) and red (red curves) galaxies at $z = 0.2$. The black triangle represents the lower limit of star-forming galaxies from observations of Tumlinson et al. (2011a). The horizontal blue and red dot-dashed lines are the amount of warm gas that the respective star formation rate can possibly produce. An additional data point for cold ($T < 10^5$ K) gas in early-type galaxies within 150 kpc is plotted as the red square with error bars indicating an estimated vertical range from the observations of Thom et al. (2012) based on 15 early-type galaxies.

(A color version of this figure is available in the online journal.)

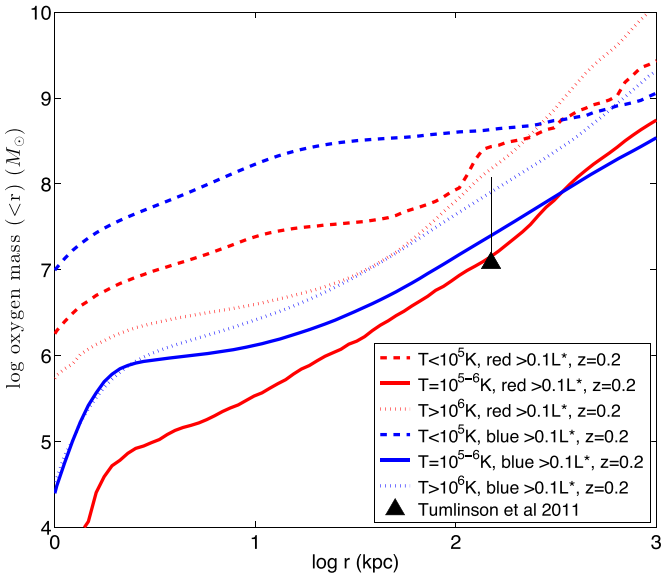

Figure 6. Cumulative metal mass as a function of radius for cold (dashed lines), warm-hot (solid lines), and hot gas (dotted lines) around blue (blue lines) and red (red lines) galaxies at $z = 0.2$.

(A color version of this figure is available in the online journal.)

The ratio of SFR_b to SFR_r can be computed directly in the simulations and was found to be 8.4. Rounding it down to 8 and combining it with Equation (2) gives us:

$$S_b/S_r = 8. \quad (4)$$

Finally, a direct assessment of the relative strength of gravitational heating of warm gas in blue and red galaxies is obtained by making the following ansatz: the amount of hot $T \geqslant 10^6$ K gas is proportional to the overall heating rate, to which the gravitational heating rate of warm gas is proportional. Figure 5 shows the gas mass of the three halo gas components interior to the radius shown in the x-axis. Within the galactocentric radius of 150 kpc, we found that the amount of hot halo gas per red $\geqslant 0.1\ L_*$ galaxy is twice that per blue $\geqslant 0.1\ L_*$ galaxy:

$$G_r/G_b = 2. \quad (5)$$

Solving Equations (3), (4), and (5) yields

$$S_b = 24/5, G_b = 1/5;$$
$$S_r = 3/5, G_r = 2/5. \quad (6)$$

The estimate given in Equation (5) is admittedly uncertain. Therefore, an estimate of how much conclusions depend on it is instructive. We find that if we had used $G_r/G_b = 1$ (instead of 2), we would have obtained $S_b = 32/7, G_b = 3/7, S_r = 4/7, G_r = 3/7$; had we used $G_r/G_b = 1/2$, we would have obtained $S_b = 4, G_b = 1, S_r = 1/2, G_r = 1/2$. Thus, a relatively robust conclusion for the sources of warm halo gas emerges: (1) for red $\geqslant 0.1\ L_*$ galaxies, $(F_r + A_r)$ and G_r have the same magnitude, and (2) for blue $\geqslant 0.1\ L_*$ galaxies, $(F_b + A_b)$ overwhelmingly dominates over G_b.

It is prudent to test the conclusion that star formation feedback may dominate the heating of warm gas that produces the observed O VI absorbers in blue galaxies. In Figure 5, the horizontal blue dot-dashed line is obtained by assuming a Chabrier-like IMF that is used in the simulations, which translates into $2/3 \times 10^{-5}$ SFR $\times\ t_{\rm cool} \times c^2/(k10^{5.5}\ {\rm K})$, where c is the speed of light and k is the Boltzmann constant; also assumed is that 2/3 of the initial supernova energy is converted into gas thermal energy, which is the asymptotic value for Sedov explosions, SFR is the respective average SFR per $\geqslant 0.1\ L_*$ blue galaxy, and $t_{\rm cool} = 6 \times 10^8$ yr is the estimated cooling time for warm halo gas. From this illustration, we see that with about 20% efficiency of heating warm gas, star formation feedback energy is already adequate for accounting for all the observed warm gas around blue galaxies. We therefore conclude that the required energy from star formation feedback to heat up the warm gas is available and our conclusions are self-consistent, even if the direct accretion contribution is zero, which we will show is not. Our results on warm gas mass are also in reasonable agreement with observations by Tumlinson et al. (2011a), as is the oxygen mass contained in the warm component, as shown in Figure 6.

We now determine F_r and A_r (F_b and A_b) individually in the following way. We compute the warm metal mass that has inward and outward radial velocities within a radial shell at $r = [50, 150]$ kpc separately for all red $>0.1\ L_*$ galaxies and all blue $>0.1\ L_*$ galaxies, denoting inflow warm metal mass as $M_Z(v_r < 0)$ and outflow warm metal mass as $M_Z(v_r > 0)$, where v_r is the radial velocity of a gas element with positive being outflowing and negative being inflowing. We define the inflow warm metal fraction as $f_{\rm in} \equiv M_Z(v_r < 0)/(M_Z(v_r < 0)+M_Z(v_r > 0))$, which is listed as the first of the three elements in each entry in Table 1 under column $|v_r| > 0$ km s^{-1}. We also compute the mean metallicities (in solar units) for the inflow and outflow warm gas, which are the second and third of the three elements in each entry in Table 1. Four separated cases are given: (1) red galaxies in the C run (C red), (2) red galaxies in the V run (V red), (3) blue galaxies in the C run (C blue), and (4) blue galaxies in the V run (V blue). In order to make sure that inflow and outflow are not confused with random motions

Table 1
Warm Inflow and Outflow at the r = [50–150] kpc Radial Shell

	$\lvert v_r\rvert > 0\,\mathrm{km\,s^{-1}}$	$\lvert v_r\rvert > 100\,\mathrm{km\,s^{-1}}$	$\lvert v_r\rvert > 250\,\mathrm{km\,s^{-1}}$
	$(f_{\rm in}, Z_{\rm in}/Z_\odot, Z_{\rm out}/Z_\odot)$	$(f_{\rm in}, Z_{\rm in}/Z_\odot, Z_{\rm out}/Z_\odot)$	$(f_{\rm in}, Z_{\rm in}/Z_\odot, Z_{\rm out}/Z_\odot)$
C red	(58%, 0.27, 0.17)	(58%, 0.29, 0.17)	(59%, 0.31, 0.17)
V red	(51%, 0.21, 0.29)	(61%, 0.18, 0.26)	(65%, 0.11, 0.33)
C blue	(54%, 0.099, 0.10)	(55%, 0.099, 0.10)	(55%, 0.099, 0.10)
V blue	(52%, 0.10, 0.14)	(52%, 0.09, 0.16)	(46%, 0.08, 0.24)

Notes. The first column gives a letter label for each run. The second, third, and fourth columns show the comoving box size, comoving spatial resolution, and dark matter particle mass. The last column indicates the GSW strength.

of gas in a Maxwellian-like distribution, we separately limit the magnitude of infall and outflow radial velocities to greater than 100 km s^{-1} and 250 km s^{-1} and list the computed quantities under the third column $|v_r| > 100$ km s^{-1} and the fourth column $|v_r| > 250$ km s^{-1}, respectively.

It is interesting to first take a closer look at the difference in metallicities between inflow and outflow gas. The warm inflow gas in red galaxies in the C run has consistently higher metallicity than warm outflow gas, $Z_{\rm in} = (0.27\text{–}0.31)Z_\odot$ versus $Z_{\rm out} = 0.17\ Z_\odot$. The opposite holds for red galaxies in the V run: $Z_{\rm in} = (0.11\text{–}0.21)\ Z_\odot$ versus $Z_{\rm out} = (0.26\text{–}0.33)\ Z_\odot$. The warm inflow gas in blue galaxies in the C run has almost the same metallicity as warm outflow gas at $Z = (0.09\text{–}0.1)\ Z_\odot$. The warm inflow gas in blue galaxies in the V run, on the other hand, has a substantially lower metallicity than the warm outflow gas, $Z_{\rm in} = (0.08\text{–}0.10)\ Z_\odot$ versus $Z_{\rm out} = (0.14\text{–}0.24)\ Z_\odot$. Except in the case of C blue, we note that the inflow and outflow gas has different metallicities, with the difference being larger when a higher flow velocity is imposed in the selection. This difference in metallicity demonstrates that the warm inflows and outflows are distinct dynamical entities, not random motions in a well-mixed gas, making our distinction of inflows and outflows physically meaningful. A physical explanation for these metallicity trends can be made as follows. In a low-density environment (i.e., in the V run) CGM has not been enriched to a high level and hot gas is not prevalent. As a result, warm (and possibly cold) inflows of relatively low metallicities still exist at low redshift. The progression from blue to red galaxies in the V run reflects a progression from very low density regions (i.e., true voids) to dense filaments and group environments, with higher metallicities for both inflows and outflows in the denser environments in the V run, but the difference between inflow and outflow metallicities remains. For red galaxies in high-density environments (C run) the CGM has been enriched to higher metallicities. Higher cooling rates of higher-metallicity gas in relatively hot environments preferentially produce higher-metallicity warm gas that originates from hot gas and has now cooled to become warm gas. The blue galaxies in the C run are primarily in cosmic filaments and the metallicity of the inflow gas is about $0.1\ Z_\odot$, which happens to coincide with the metallicity of the outflow gas. One needs to realize that at the radial shell r = [50–150] kpc over which the tabulated quantities are computed, the outflow gas originated in star-forming regions has loaded a substantial amount of interstellar and CGM in the propagation process.

Let us now turn to the warm inflow and outflow metal mass. It appears that the fraction of inflow warm metals (out of all warm metals) lies in a relatively narrow range of $f_{\rm in} = 45\%\text{–}65\%$. For our present purpose we will just say $F_r = A_r$ and $F_b = A_b$. Armed with these two relations our best estimates for various contributions to the observed warm halo metals, as a good proxy for the O VI absorption, can be summarized as follows.

1. For red $\geqslant 0.1\ L_*$ galaxies at $z = 0.2$, contributions to warm metals in the halo gas from star formation feedback (F_r), accretion of intergalactic medium (A_r), and gravitational shock heating (G_r) are $(F_r, A_r, G_r) = (30\%, 30\%, 40\%)$.
2. For blue $\geqslant 0.1\ L_*$ galaxies at $z = 0.2$ contributions to warm metals in the halo gas from the three sources are $(F_b, A_b, G_b) = (48\%, 48\%, 4\%)$.
3. Dependencies of warm halo gas metallicities on galaxy type and environment are complex but physically understandable. For red galaxies, the metallicity of inflowing warm gas increases with increasing environmental overdensity, whereas that of outflowing warm gas decreases with increasing environmental overdensity. For blue galaxies, the metallicity of inflowing warm gas depends very weakly on environmental overdensity, whereas that of outflowing warm gas decreases with increasing environmental overdensity. As a whole, the mean metallicity of warm halo gas in red galaxies is $\sim 0.25\ Z_\odot$, while that of blue galaxies is $\sim 0.11\ Z_\odot$.

We suggest that these estimates of source fractions are not seriously in error on average, if one is satisfied with an accuracy of a factor of two. The relative metallicity estimates should be quite robust with errors much smaller than a factor of two. We stress that these estimates are averaged over many red and blue galaxies and correlations (such as between warm gas mass and SFR) do not hold strictly for individual galaxies. Rather, we expect large variations from galaxy to galaxy, even at a fixed SFR. Figure 7 makes this important point clear and shows that, while there is a positive correlation between warm metal mass within a 150 kpc radius and SFR for galaxies with non-negligible SFR (i.e., appearing in the SFR range shown), a dispersion of ~ 1 dex in warm metal mass at a fixed SFR in the range of 0.1–100 $M_\odot$ yr^{-1} exists. The goodness of the fit can be used as a way to rephrase this significant dispersion. If one assumes that the error bar size of each log mass determination for each shown galaxy is 1, one finds that the χ square per degree of the fitting line (green) is 0.80, indicating that the correlation between $\log M_Z(T = 10^{5-6}\ \mathrm{K})$ and $\log \mathrm{SFR}$ is only good to about 1 dex in warm metal gas mass.

3.4. Composition of Low-z Halo Gas

In Cen (2012a), we show that the properties of O VI absorption lines at low redshift, including their abundance, Doppler-width-column density distribution, temperature range, metallicity, and coincidence between O VII and O VI lines, are all in good agreement with observations (Danforth & Shull 2008; Tripp et al. 2008; Yao et al. 2009). In the above we have shown that O VI–galaxy relations as well as oxygen mass in galaxies in the

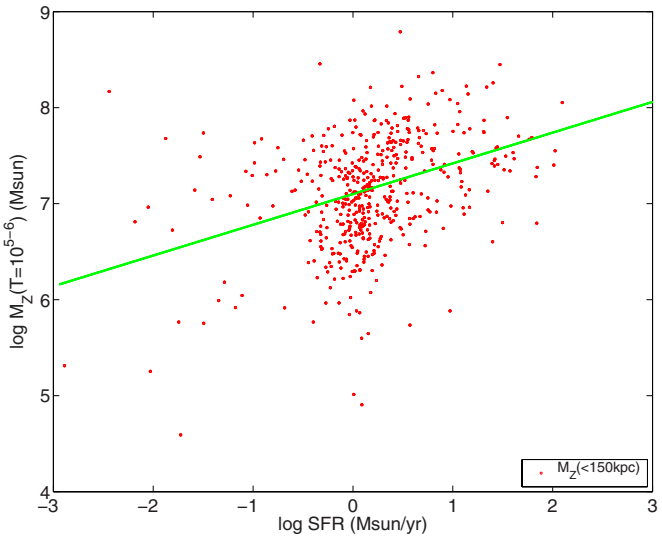

Figure 7. Metal mass in the warm gas M_Z within a galactocentric radius of 150 kpc as a function of the SFR of the galaxy at $z = 0.2$. Each red dot is a galaxy. The green curve shows the best linear regression, $\log M_Z(T = 10^{5-6}\ \mathrm{K})/M_\odot = 0.32 \log \mathrm{SFR} + 7.1$, for the galaxies shown.

(A color version of this figure is available in the online journal.)

simulations are also in excellent agreement with observations. These tests together are non-trivial and lend us significant confidence to now examine the overall composition of halo gas at low-z.

Figure 8 shows the differential (left panel) and cumulative (right panel) mass fractions of each gas component as a function of galactocentric distance for red (red curves) and blue (blue curves) galaxies. We note that the fluctuating behaviors (mostly in the differential functions on the left panel) are due to occasional dense cold clumps in neighboring galaxies. Overall, we see that, within about (10, 30) kpc for (red, blue) galaxies, the cold ($T < 10^5$ K) gas component completely dominates, making up about (80%, >95%) of all gas at these radii. For both >0.1 L_* (red, blue) galaxies, cold gas remains the major component up to $r = (30, 150)$ kpc, within which its mass comprises 50% of all gas. At $r > (30, 200)$ kpc for (red, blue) galaxies the hot ($T > 10^6$ K) gas component dominates. The warm gas component, while having been extensively probed observationally, appears to be a minority in both red and blue galaxies at all radii. The warm component's contribution to the overall gas content reaches its peak value of ~30% at $r = 100$–300 kpc for blue galaxies, whereas in red galaxies it is negligible at $r < 10$ kpc and hovers around the 5% level at $r = 30$–1000 kpc. The prevalence of cold gas at small radii in red (i.e., low star formation activities) galaxies is intriguing and perhaps surprising to some extent. Some recent observations indicate that early-type galaxies in the real universe do appear to contain a substantial amount of cold gas, consistent with our findings. For example, Thom et al. (2012) infer a mean mass of 10^9–$10^{11}\ M_\odot$ of gas with $T < 10^5$ K at $r < 150$ kpc based on a sample of 15 early-type galaxies at low redshift from COS observations, which is shown as the red square (its horizontal position is slightly shifted to the right for display clarity) in Figure 5. Their inferred range is in fact consistent with our computed value of $\sim 6 \times 10^{10}\ M_\odot$ of cold $T < 10^5$ K gas for red >0.1 L_* galaxies, shown as the red dashed line in Figure 5.

Figure 9, which is analogous to Figure 8, shows the corresponding distributions for metal mass fractions in the three components for red and blue galaxies. The overall trends are similar to those for total warm gas mass. We note one significant difference here. The overall dominance of metal mass in cold gas extends further out radially for both red and blue galaxies, whereas the contributions to metal mass from the other two components are compensatorily reduced. For example, we find that the radius within which the cold mass component makes up 50% of total gas in (red, blue) galaxies is (40,150) kpc, whereas the radius within which the cold mass component makes up 50% of total gas metals in (red, blue) galaxies becomes (200, 500) kpc. This is largely due to a significantly higher metallicity of the cold component in both red and blue galaxies compared to the other two components, as shown in Figure 10. We also note from Figure 10 that the warm gas in red galaxies has a higher metallicity than in blue galaxies, as found earlier, with the mean metallicity (~0.25 $Z_\odot$, ~0.11 $Z_\odot$) in (red, blue) galaxies within a radius of 150 kpc.

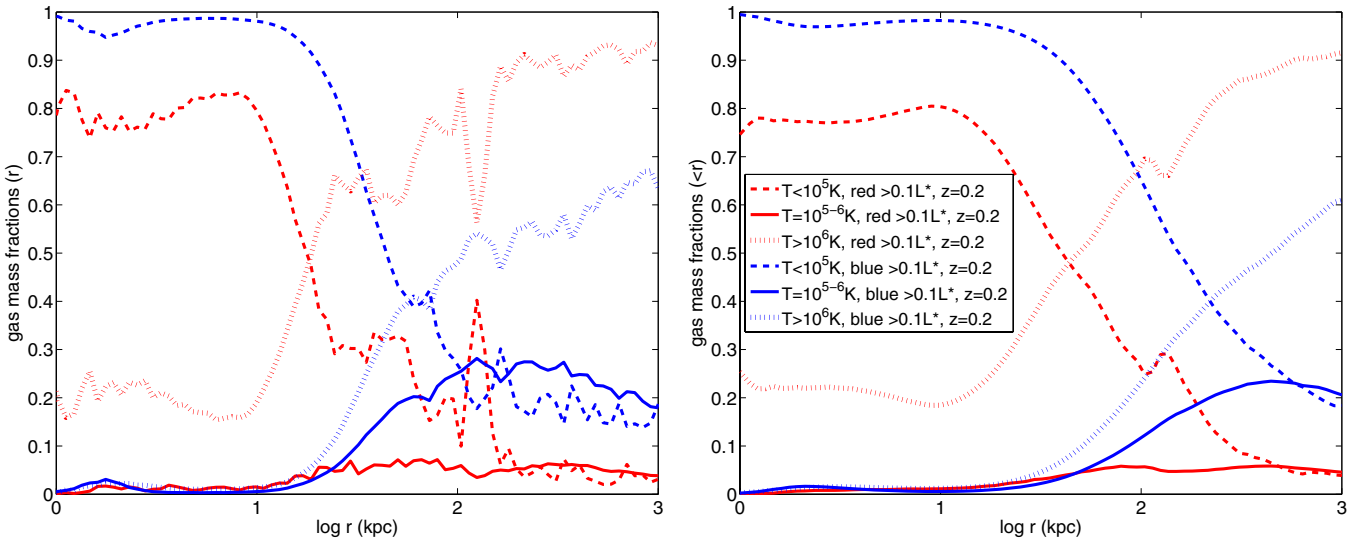

Figure 8. Differential (left panel) and cumulative (right panel) gas mass fractions as a function of radius for cold (dashed curves), warm-hot (solid curves), and hot gas (dotted curves) around blue (blue curves) and red (red curves) >0.1$L*$ galaxies at $z = 0.2$.

(A color version of this figure is available in the online journal.)

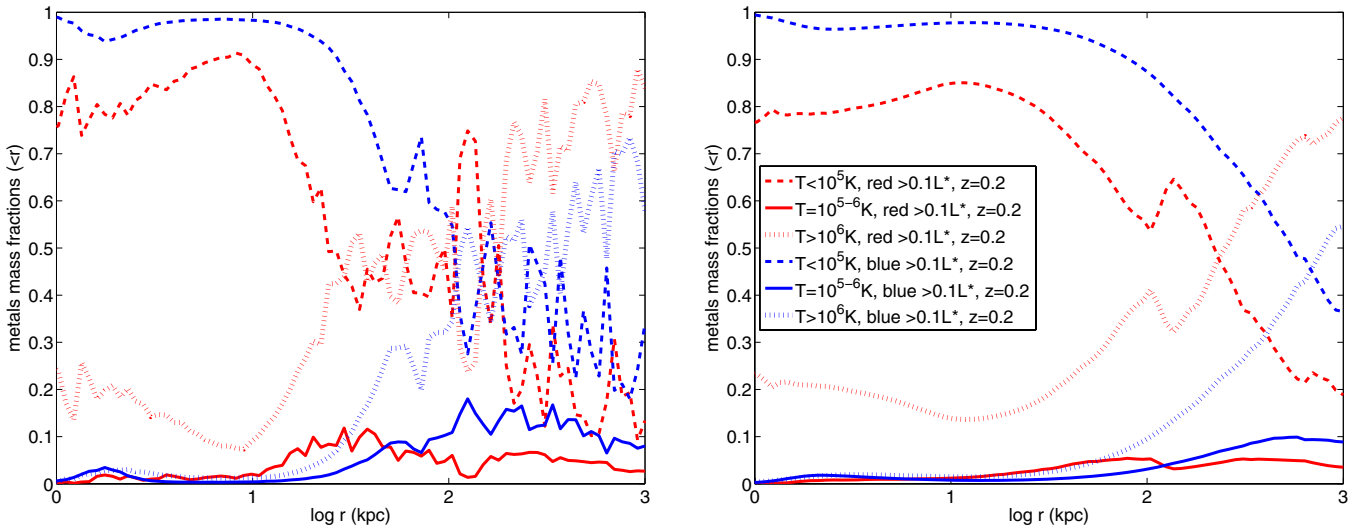

Figure 9. Differential (left panel) and cumulative (right panel) gas metal mass fractions as a function of radius for cold (dashed lines), warm-hot (solid lines), and hot gas (dotted lines) around blue (blue lines) and red (red lines) galaxies at $z = 0.2$.

(A color version of this figure is available in the online journal.)

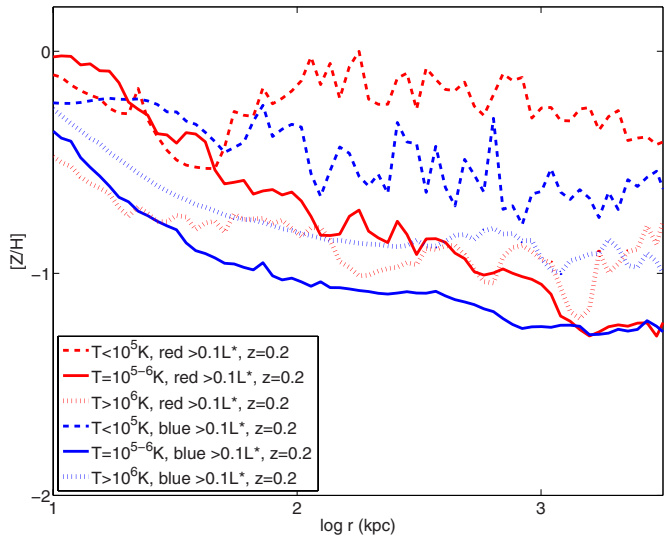

Figure 10. Metallicity for cold (dashed lines), warm-hot (solid lines), and hot gas (dotted lines) around blue (blue lines) and red (red lines) galaxies at $z = 0.2$ as a function of radius.

(A color version of this figure is available in the online journal.)

4. CONCLUSIONS

The distribution and evolution of the IGM have largely been addressed by cosmological simulations (e.g., Cen & Ostriker 1999; Davé et al. 2001; Cen & Chisari 2011; Cen 2012a). The global distribution and composition of halo gas in and around galaxies at low redshift ($z < 0.5$) are addressed here, utilizing state-of-the-art high-resolution ($460\,h^{-1}$ pc), large-scale cosmological hydrodynamic simulations with validated star formation and feedback prescriptions.

We find that within about (10, 30) kpc for (red, blue) $>0.1\ L_*$ galaxies the cold ($T < 10^5$ K) gas component is the primary gas component making up about (80%, >95%) of all gas. For both $>0.1\ L_*$ (red, blue) galaxies, cold gas remains the major component up to $r = (30, 150)$ kpc, within which its mass comprises 50% of all gas. At $r > (30, 200)$ kpc for (red, blue) galaxies, the hot ($T > 10^6$ K) gas component dominates. The warm ($T = 10^5$–10^6 K) gas component makes a minor contribution to the overall gas mass as well as to the gas metal mass in both red and blue galaxies. The warm component's contribution to the overall gas content reaches its peak value of ∼30% at $r = 100$–300 kpc for blue galaxies, whereas in red galaxies its contribution is negligible at $r < 10$ kpc and capped at the 5% level at $r = 30$–1000 kpc. Where comparisons with observations are possible, we find that the amount of warm gas and oxygen mass in star-forming galaxies is in agreement with observations (e.g., Tumlinson et al. 2011b), so is the amount of cold gas in early-type galaxies at low redshift (e.g., Thom et al. 2012). The presence of a significant amount of cold gas in red galaxies at low redshift is new and somewhat surprising. The nature of this cold gas and its role in star formation in red galaxies are not addressed in the present paper. This and signatures of the predicted dominance of hot gas in blue galaxies (as well as red galaxies) at large radii will be addressed elsewhere.

In addition to the agreement between our simulations and observations with respect to the global O VI incidence rate (Cen 2012a), we show that our predicted correlations between galaxies and strong O VI absorbers of column density $N_{\rm O\,VI} \geqslant 14$ cm^{-2} are in excellent agreement with observations with χ square per degree of freedom equal to 1.2. On the other hand, when we use only photoionized O VI absorbers ($T < 3 \times 10^4$ K) in the simulations, the comparisons between simulations and observations become substantially less favorable with χ^2 per degree of freedom equal to 7.6; the significant disagreement stems from the photoionized O VI absorbers being too distant from galaxies. The O VI line incidence rate per $\geqslant 0.1\ L_*$ galaxy around blue ($g - r < 0.6$) galaxies in our simulations is higher than that around $\geqslant 0.1\ L_*$ red ($g - r > 0.6$) galaxies by a factor of ∼4 at $r \leqslant 100$–300 kpc, increasing to $\geqslant 10$ at $r \leqslant 20$ kpc, in reasonable agreement with extant observations (e.g., Chen & Mulchaey 2009; Prochaska et al. 2011a), whereas in the photoionization-dominated model the ratio is zero at $r < 100$ kpc. Thus, the cross-correlations between galaxies and O VI lines provide powerful differentiation between collisional and photoionization models, with collisional ionization dominance for strong ($N_{\rm O\,VI} \geqslant 10^{14}$ cm^{-2}) O VI absorbers being currently favored.

The O VI-bearing halo gas (i.e., the warm component) is found to be *"transient"* in nature and hence requires constant sources. We perform analysis to unravel the sources and their relations to galaxy formation. We find that, on average, to within a factor of two, contributions to warm metals in the halo gas from star formation feedback (F_r), accretion of intergalactic medium (A_r), and gravitational shock heating (G_r) are $(F_r, A_r, G_r) = (30\%, 30\%, 40\%)$ for red $\geqslant 0.1\ L_*$ galaxies at $z = 0.2$. For blue $\geqslant 0.1\ L_*$ galaxies at $z = 0.2$ contributions are $(F_b, A_b, G_b) = (48\%, 48\%, 4\%)$. For both red and blue galaxies, the amounts of warm gas in inflows and outflows are comparable. The mean metallicity of warm halo gas in (red, blue) galaxies is ($\sim 0.25\ Z_\odot$, $\sim 0.11\ Z_\odot$). Environmental dependence of O VI-bearing halo gas is as follows. In low-density environments, the metallicity of inflowing warm gas is substantially lower than that of outflowing warm gas; the opposite is true in high-density environments.

I thank Dr. M. K. R. Joung for help in generating the initial conditions for the simulations and in running a portion of the simulations, Greg Bryan for help with the Enzo code, Drs. John Wise and Matthew Turk for very useful help with the analysis program (Turk et al. 2011), and an anonymous referee for constructive feedback. Computing resources were in part provided by the NASA High-End Computing (HEC) Program through the NASA Advanced Supercomputing (NAS) Division at Ames Research Center. The research is supported in part by NASA grant NNX11AI23G.

REFERENCES

Allen, S. W., Rapetti, D. A., Schmidt, R. W., et al. 2008, MNRAS, 383, 879
Astier, P., Guy, J., Regnault, N., et al. 2006, A&A, 447, 31
Bahcall, N. A., Ostriker, J. P., Perlmutter, S., & Steinhardt, P. J. 1999, Sci, 284, 1481
Benson, A. J., Bower, R. G., Frenk, C. S., et al. 2003, ApJ, 599, 38
Berlind, A. A., & Weinberg, D. H. 2002, ApJ, 575, 587
Blanton, M. R., Hogg, D. W., Bahcall, N. A., et al. 2003, ApJ, 592, 819
Bond, J. R., Cole, S., Efstathiou, G., & Kaiser, N. 1991, ApJ, 379, 440
Bruzual, G., & Charlot, S. 2003, MNRAS, 344, 1000
Bryan, G. L. 1999, Comput. Sci. Eng., 1, 46
Bryan, G. L., & Norman, M. L. 1999, in Structured Adaptive Mesh Refinement Grid Methods, ed. N. P. C. S. B. Baden (IMA Volumes on Structured Adaptive Mesh Refinement Methods, Vol. 117; New York: Springer-Verlag), 165
Bullock, J. S., Kolatt, T. S., Sigad, Y., et al. 2001, MNRAS, 321, 559
Cen, R. 2011, ApJ, 741, 99
Cen, R. 2012a, ApJ, 753, 17
Cen, R. 2012b, ApJ, 748, 121
Cen, R., & Chisari, N. E. 2011, ApJ, 731, 11
Cen, R., Kang, H., Ostriker, J. P., & Ryu, D. 1995, ApJ, 451, 436
Cen, R., Miralda-Escude, J., Ostriker, J. P., & Rauch, M. 1994, ApJL, 437, L9
Cen, R., Nagamine, K., & Ostriker, J. P. 2005, ApJ, 635, 86
Cen, R., & Ostriker, J. P. 1992, ApJL, 399, L113
Cen, R., & Ostriker, J. P. 1999, ApJ, 514, 1
Cen, R., & Ostriker, J. P. 2006, ApJ, 650, 560
Chen, H.-W., & Mulchaey, J. S. 2009, ApJ, 701, 1219
Cooray, A., & Sheth, R. 2002, PhR, 372, 1
Croft, R. A. C., Weinberg, D. H., Bolte, M., et al. 2002, ApJ, 581, 20
Danforth, C. W., & Shull, J. M. 2008, ApJ, 679, 194
Davé, R., Cen, R., Ostriker, J. P., et al. 2001, ApJ, 552, 473
Davé, R., Finlator, K., Oppenheimer, B. D., et al. 2010, MNRAS, 404, 1355
Diemand, J., Kuhlen, M., & Madau, P. 2007, ApJ, 657, 262
Eisenstein, D., & Hu, P. 1999, ApJ, 511, 5
Eisenstein, D. J., & Hut, P. 1998, ApJ, 498, 137
Evrard, A. E., Summers, F. J., & Davis, M. 1994, ApJ, 422, 11
Ferland, G. J., Korista, K. T., Verner, D. A., et al. 1998, PASP, 110, 761
Freedman, W. L., Madore, B. F., Scowcroft, V., et al. 2012, ApJ, 758, 24
Gnedin, N. Y., Tassis, K., & Kravtsov, A. V. 2009, ApJ, 697, 55
Governato, F., Willman, B., Mayer, L., et al. 2007, MNRAS, 374, 1479
Haardt, F., & Madau, P. 2012, ApJ, 746, 125
Heckman, T. M. 2001, in ASP Conf. Ser. 240, Gas and Galaxy Evolution, ed. J. E. Hibbard, M. Rupen, & J. H. van Gorkom (San Francisco, CA: ASP), 345
Hopkins, P. F., Hernquist, L., Cox, T. J., et al. 2006, ApJS, 163, 1
Jenkins, A., Frenk, C. S., White, S. D. M., et al. 2001, MNRAS, 321, 372
Joung, M. R., Cen, R., & Bryan, G. L. 2009, ApJL, 692, L1
Katz, N., Weinberg, D. H., & Hernquist, L. 1996, ApJS, 105, 19
Kereš, D., Katz, N., Weinberg, D. H., & Davé, R. 2005, MNRAS, 363, 2
Komatsu, E., Smith, K. M., Dunkley, J., et al. 2011, ApJS, 192, 18
Krauss, L. M., & Turner, M. S. 1995, GReGr, 27, 1137
Lacey, C., & Cole, S. 1993, MNRAS, 262, 627
Mo, H. J., & White, S. D. M. 2002, MNRAS, 336, 112
Naab, T., Johansson, P. H., Ostriker, J. P., & Efstathiou, G. 2007, ApJ, 658, 710
Oppenheimer, B. D., & Davé, R. 2006, MNRAS, 373, 1265
Oppenheimer, B. D., Davé, R., Katz, N., Kollmeier, J. A., & Weinberg, D. H. 2012, MNRAS, 420, 829
O'Shea, B. W., Abel, T., Whalen, D., & Norman, M. L. 2005, ApJL, 628, L5
Percival, W. J., Nichol, R. C., Eisenstein, D. J., et al. 2007, ApJ, 657, 645
Perlmutter, S., Aldering, G., della Valle, M., et al. 1998, Natur, 391, 51
Planck Collaboration, Ade, P. A. R., Aghanim, N., Armitage-Caplan, C., et al. 2013, arXiv:1303.5076
Prochaska, J. X., Weiner, B., Chen, H.-W., Cooksey, K. L., & Mulchaey, J. S. 2011a, ApJS, 193, 28
Prochaska, J. X., Weiner, B., Chen, H.-W., Mulchaey, J., & Cooksey, K. 2011b, ApJ, 740, 91
Rafelski, M., Wolfe, A. M., Prochaska, J. X., Neeleman, M., & Mendez, A. J. 2012, ApJ, 755, 89
Rauch, M., Miralda-Escude, J., Sargent, W. L. W., et al. 1997, ApJ, 489, 7
Riess, A. G., Filippenko, A. V., Challis, P., et al. 1998, AJ, 116, 1009
Riess, A. G., Macri, L., Casertano, S., et al. 2011, ApJ, 730, 119
Seljak, U., Makarov, A., McDonald, P., et al. 2005, PhRvD, 71, 103515
Shen, Y., & Kelly, B. C. 2010, ApJ, 713, 41
Sheth, R. K., & Tormen, G. 1999, MNRAS, 308, 119
Shull, J. M., Roberts, D., Giroux, M. L., Penton, S. V., & Fardal, M. A. 1999, AJ, 118, 1450
Shull, J. M., Smith, B. D., & Danforth, C. W. 2012, ApJ, 759, 23
Smith, B. D., Hallman, E. J., Shull, J. M., & O'Shea, B. W. 2011, ApJ, 731, 6
Somerville, R. S., & Primack, J. R. 1999, MNRAS, 310, 1087
Tegmark, M., Strauss, M. A., Blanton, M. R., et al. 2004, PhRvD, 69, 103501
Tepper-García, T., Richter, P., Schaye, J., et al. 2011, MNRAS, 413, 190
Teyssier, R. 2002, A&A, 385, 337
Thom, C., Tumlinson, J., Werk, J. K., et al. 2012, ApJL, 758, L41
Tonnesen, S., & Cen, R. 2012, MNRAS, 425, 2313
Tornatore, L., Borgani, S., Viel, M., & Springel, V. 2010, MNRAS, 402, 1911
Tripp, T. M., Meiring, J. D., Prochaska, J. X., et al. 2011, Sci, 334, 952
Tripp, T. M., Sembach, K. R., Bowen, D. V., et al. 2008, ApJS, 177, 39
Tumlinson, J., Thom, C., Werk, J. K., et al. 2011a, Sci, 334, 948
Tumlinson, J., Werk, J. K., Thom, C., et al. 2011b, ApJ, 733, 111
Turk, M. J., Smith, B. D., Oishi, J. S., et al. 2011, ApJS, 192, 9
Wechsler, R. H., Bullock, J. S., Primack, J. R., Kravtsov, A. V., & Dekel, A. 2002, ApJ, 568, 52
Wiersma, R. P. C., Schaye, J., & Smith, B. D. 2009, MNRAS, 393, 99
Yao, Y., Tripp, T. M., Wang, Q. D., et al. 2009, ApJ, 697, 1784
Zheng, Z., Coil, A. L., & Zehavi, I. 2007, ApJ, 667, 760